# Giant photoinduced lattice distortion in oxygen vacancy ordered SrCoO$_{2.5}$ thin films

Bingbing Zhang [1,*] Xu He,[2] Jiali Zhao,[1] Can Yu,[1] Haidan Wen,[3] Sheng Meng,[4] Eric Bousquet,[2] Yuelin Li,[3] Chen Ge,[4] Kuijuan Jin,[4] Ye Tao,[1,†] and Haizhong Guo[5,‡]

[1]*Institute of High Energy Physics, Chinese Academy of Sciences, Beijing 100049, China*
[2]*Physique Théorique des Matériaux, Q-MAT, CESAM, Université de Liège, B-4000 Liège, Belgium*
[3]*Advanced Photon Source, Argonne National Laboratory, Argonne, Illinois 60439, USA*
[4]*Institute of Physics, Chinese Academy of Sciences, Beijing 100190, China*
[5]*School of Physics and Microelectric, Zhengzhou University, Zhengzhou 450001, China*

Despite the progress in understanding the formation and migration of oxygen vacancies in strongly correlated complex oxides, few studies focused on the dynamic behaviors of the oxygen vacancies under the transient and nonequilibrium states. Here we report a series of multitimescale ultrafast x-ray diffraction experiments using picosecond synchrotron and femtosecond table-top x-ray sources to monitor the structural dynamics in oxygen-vacancy-ordered SrCoO$_{2.5}$ thin films excited by photons. A giant photoinduced structure distortion in the $c$-axis direction (with strain $\Delta c/c > 1\%$) was observed, higher than any previously reported data in the other transition metal oxide films. The femtosecond x-ray diffraction reveals the formation and propagation of the coherent acoustic phonons, indicating an instantaneous and a much larger photoinduced stress within the first 100 ps. Density functional theory reproduced the photostrictive responses and the strong dependence on excitation wavelength as observed in the experiments. The combined experimental and theoretic results demonstrate that the photoexcitation of the bonding to antibonding states via charge transfer is the dominant mechanism in the SrCoO$_{2.5}$ thin films, distinct from the depolarization effect by photoinduced carriers in the other perovskite oxides.

## I. INTRODUCTION

Multivalent transition-metal oxides possess intriguing physical properties and potential in energy applications [1,2]. Among them Co-based perovskite SrCoO$_{3-x}$ are the most promising candidates for solar thermochemical energy storage application. With the variation of the oxygen stoichiometry, the physical properties of SrCoO$_{3-x}$ can be reversible transferred between two topotactic phases, ferromagnetic metal perovskite SrCoO$_3$ and antiferromagnetic insulator brownmillerite SrCoO$_{2.5}$ (BM-SCO). In particular, the long-range ordering of the oxygen vacancies and rich polyhedral configurations make BM-SCO very interesting for fundamental research and promising for applications of the enhancement of the efficacy of electrocatalysts and the development of solid oxide fuel cells [3–7]. The ordered oxygen vacancies in BM-SCO result in the supertetragonality of the Co-O tetrahedron layer, which suppresses the tilting of Co-O octahedron layer, like the ferroelectrics of BaTiO$_3$ and PbTiO$_3$, where the tilting of octahedron is usually suppressed due to the competition with polarization [8]. Although the physical properties of BM-SCO as a function of strain [9,10], pressure [11], external field [12,13], and heating [4,6] have been widely investigated, its dynamic behavior under transient photoexcitation has not been reported.

Here we present the ultrafast x-ray diffraction (UXRD) measurements of the BM-SCO thin films with both picosecond and femtosecond temporal resolutions, in combination with first-principles calculations. The UXRD technique has been proven to be a powerful tool in interrogating transient phenomena upon photoexcitation in materials including Sr$_2$IrO$_4$ [14], PbTiO$_3$ [15], and BiFeO$_3$ [16,17]. In our experiments, the structural dynamics as a result of excitation at different photon energies was monitored. A giant out-of-plane strain ($\Delta c/c > 1\%$) was observed, which is much larger at 3.1-eV photon energy than that at 1.55-eV photon energy. This strong excitation photon energy dependence is also reproduced by density functional theory (DFT) simulation assuming the lattice distortion arise from the charge transfer (CT) induced by the photon excitation.

## II. EXPERIMENTAL RESULTS

### A. Static characterizations

Figure 1(a) shows the brownmillerite structure of BM-SCO with alternating Co-O octahedral and tetrahedral layers stacked along the [001] direction and ordered oxygen vacancy channels arranged in the *a*-*b* plane. The BM-SCO films were grown on the (001) LaAlO$_3$ (LAO) substrates by pulsed laser deposition technique, deposited at 700 °C using an excimer XeCl laser (1.5 J/cm$^2$, 308 nm, 2 Hz) under the oxygen

*zhangbb@ihep.ac.cn
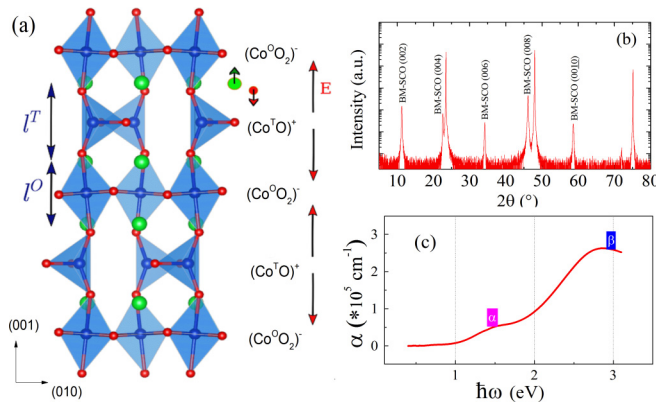†taoy@ihep.ac.cn
‡hguo@zzu.edu.cn

FIG. 1. (a) The crystal structure of BM-SCO, with internal electric field due to the charged-layer structure, where the superscripts T and O represent the Co atom in a tetrahedral and octahedral cell, respectively. (b) The XRD $\theta$-$2\theta$ pattern of a 46-nm-thick BM-SCO thin film on a LAO substrate. (c) Optical absorption of the BM-SCO film with two characterized peaks at 1.4 eV ($\alpha$) and 2.8 eV ($\beta$), the pump photon energies used in this work are labeled with arrows.

pressure of 10 Pa. After deposition, the films were *in situ* annealed for 30 min and then cooled down slowly to room temperature. Figure 1(b) shows the XRD $\theta$-$2\theta$ scan pattern of the film at 8-keV photon energy, indicating the high quality of the sample. Besides the ordinary (004) and (008) reflections close to the substrate peaks, there also exist characteristic Bragg peaks of (002), (006), and (0010) reflections, originating from the altered Co-O octahedral and tetrahedral layers. The big lattice mismatch (2.98%) between the substrate ($c =$ 3.792 Å) and the film ($c =$ 3.905 Å), introduces an in-plane compressive strain into the BM-SCO film. The film thickness we chosen is 46 nm, just above the critical point of 40 nm, where the in-plane strain is completely released [10].

The optical absorption spectrum of the sample was obtained from the transmittance measurements basing on a spectrophotometer (Agilent Cary 7000), as shown in Fig. 1(c). Two characteristic peaks marked as $\alpha$ and $\beta$, represent the *d-d* transition between octahedral Co 3*d* states and the *p-d* transition between O 2*p* and mostly octahedral Co 3*d* states, respectively [3]. The direct band gap ($\sim$2.18 eV) and Mott gap ($\sim$0.32 eV) of the BM-SCO film can also be derived from the optical absorption data by plotting $\alpha(\omega)^{1/2}$ and making the tangent lines near the $\alpha$ and $\beta$ peaks [3,13]. The penetration depths $\zeta$ at different excitation photon energies are measured to be 29 nm (3.1 eV) and 100 nm (1.55 eV).

### B. Synchrotron based UXRD experiment

The UXRD measurements were first performed on the BM-SCO film at 7-ID-C beamline of Advance Photon Source with picosecond time resolution. The film thickness $d =$ 46 nm was precisely derived from the oscillations of the x-ray reflectivity. The 50-femtosecond (fs) laser pulses from the Ti-sapphire laser system (Coherent Legend) at a repetition rate of 1 kHz were used to illuminate the sample at an incident angle of 45° and an elliptical footprint of 970 $\mu$m $\times$ 400 $\mu$m full width half maximum (FWHM). The optical excitations were provided by the fundamental output of the
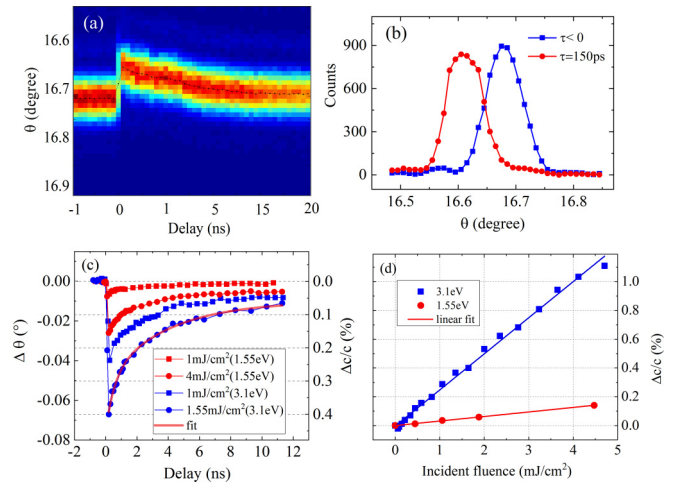


FIG. 2. (a) Diffraction intensity distribution upon the excitation of 3.1-eV laser pulses with incident fluence of 1.55 mJ/cm$^2$. (b) $\theta$-$2\theta$ scans of the BM-SCO (008) reflection before and after excitation. (c) The extracted angular shift of (008) peak and the corresponding strain as a function of time at different pump fluence and photon energies, one of which is empirically fitted to a biexponential decay function. (d) Photoinduced strain at $\tau = 150$ ps as a function of incident fluence upon excitation of 3.1- and 1.55-eV laser pulses, together with a linear fit to the data.

laser system (1.55 eV) and its frequency doubling output (3.1 eV). The monochromatic x-ray beam ($\Delta E/E \sim 0.01\%$) at a photon energy of 11 keV was focused into a 50-$\mu$m FWHM spot center in the optical illuminated area. The probed x-ray bunches synchronized to the pump laser pulses were then gated out by an area Detector (Pilatus 100k, Detectris).

The angular intensity distribution of the BM-SCO (008) reflection was measured after the laser excitation (3.1 eV, 1.55 mJ/cm$^2$) as a function of time, as shown in Fig. 2(a). The angular shift to the smaller Bragg angle at $\tau = 150$ ps, as shown in Fig. 2(b), corresponds to an out-of-plane expansion of $\Delta c/c = 0.4\%$. Unlike the giant change of the diffraction angle, the width of the diffraction peak remains unchanged after photoexcitation, indicating a homogeneous spatial strain profile at the given temporal scale. Figure 2(c) also gives the photoinduced strains at various pump photon energies and incident fluence. The angular shift excited by 3.1-eV pump pulses is much bigger than that by the 1.55-eV case. Taking the two 1 mJ/cm$^2$ cases into consideration, e.g., the maximum angular shift for the 3.1-eV case is about 6 times larger than that for the 1.55-eV case. The angular dynamics was fitted to a biexponential decay function, indicating a fast time constant of 0.45 ns and a slow time constant of 4.3 ns, as shown in Fig. 2(c). A linear fluence dependence of the angular shift at $\tau = 150$ ps on the incident fluence was observed for both photon energies [as shown in Fig. 2(d)], showing a maximum strain of $\sim$1% for the 3.1 eV case. For fluence higher than 4 mJ/cm$^2$, the strain starts to saturate, along with apparent sample degradation.

### C. Laboratory-based UXRD experiment

To provide insight into the buildup of the strain right after photoexcitation, we performed the sub-ps UXRD
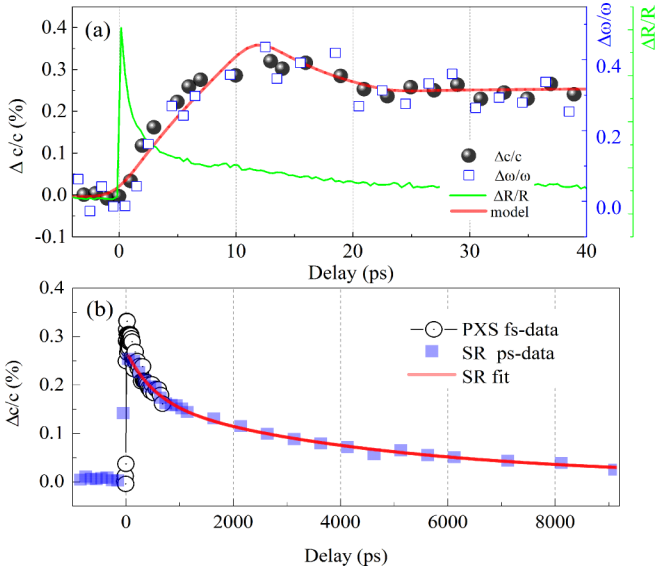
FIG. 3. (a) Photoinduced Bragg peak shift (black circle dots) and width change (blue squares) of the (008) reflection of the BM-SCO film from $-5$ to 40 ps obtained by fs-UXRD measurements, as well as the transient optical reflectivity change (green solid line) by use of dual-color spectroscopy. The red solid lines represent the simulated strains basing on the analytical photon propagation model. (b) The multiscale photoinduced strain by merging the fs and ps UXRD data after fluence calibration. The red solid line is the exponential fit to the SR data.

measurements on the same sample using a laser plasma x-ray source (PXS). PXS provides 50-fs pump laser pulses and $\sim$250-fs probe x-ray pulses at a repetition rate of 1 kHz. The temporal resolution of the UXRD setup was experimentally demonstrated by the x-ray reflectivity oscillation measurement of the well-studied $SrRuO_3/SrTiO_3$ superlattice [18]. By use of the Montel multilayer optics, only the Cu $K\alpha$ characteristic line emission ($E = 8.047$ keV, $\Delta E/E \sim 0.25\%$) was selected and focused into a 300-$\mu$m (FWHM) footprint, overfilled by a 1-mm FWHM UV illuminated area on the sample. The laser beam is incident to the film surface at an angle of 40°. Unlike the $\theta$-$2\theta$ scan configuration used at SR-based UXRD experiment, we measured the Bragg peak shift of the (008) reflection in the convergent mode [19], within the convergent angle of 0.29°. The all optical pump-probe spectroscopy was also obtained basing on the parasitic mode of PXS setup, where the pump and probe pulses are 400- and 800-nm laser pulses.

The photoinduced Bragg peak shift and width change upon 3.1-eV excitation were measured as a function of time at the absorbed fluence of 0.67 mJ/cm$^2$. Unlike the synchrotron-based measurements, significant peak width change was also observed along with the emergence of angular shift, indicating the inhomogeneous strain profile at the early time, as shown in Fig. 3(a). The lattice dynamics within the first few tens of ps can be interpreted as due to the propagation of the coherent acoustic phonons resulted from a transient photoexcited stress. The out-of-plane expansion rises to its maximum at $\tau_0 = 11.5 \pm 1$ ps and returns to a quasiequilibrium state at $\tau_1 = 22.5 \pm 1$ ps, then is superimposed by a much slower

ns scale relaxation process, as shown in Fig. 3(b). $\tau_0$ and $\tau_1$ correspond to the time that the strain front travels once and twice across the film, respectively, with a velocity of $\upsilon = d/(\tau_1 - \tau_0) = 4.2 \pm 0.3$ km/s, where $d$ refers to the thickness of the thin film. The slight difference ($\sim$0.5 ps) between $\tau_0 = 11.5$ ps and $\tau_1 - \tau_0 = 11$ ps implies an ultrafast electron-phonon coupling time in this system, in line with our dual-color pump-probe measurement, which was fitted to an bi-exponential decay function with two time constants of 0.7 and 10.6 ps, as shown in Fig. 3(a). The fast decay of 0.7 ps represents the relaxation time of photoinduced carriers to the acoustic phonons via electron-phonon coupling.

We also simulated the photoinduced strain by use of an analytical phonon propagation model, as shown is Fig. 3(a). The detail of the phonon propagation model can be found in Ref. [20]. The sound velocity $\upsilon = 4.2$ km/s, penetration depths $\zeta = 29$ nm, sample thickness $d = 46$ nm and a convoluted 250-fs Gaussian x-ray pulse are used to fit the experimental data. The derived elastic constant $C_{33} = \rho * \upsilon^2 \approx 92$ GPa using $\upsilon = 4.2$ km/s and $\rho = 5.2$ g/cm$^3$ agrees well with the reported value of $106.1 \pm 9.8$ GPa [11]. The peak shifts of the fs data collapse into the synchrotron data when scaled by their fluence differences, as shown in Fig. 3(b). We also notice that the maximum photoinduced strain of the PXS fs-data is about 1.4 times larger than that of SR ps-data, due to the better temporal resolution of PXS.

## III. DISCUSSION

Compared with the previous UXRD studies on the transition metal oxides, a smaller fluence was needed to achieve a comparable strain in the BM-SCO film, indicating much higher photostrictive efficiency. Table I summarizes the maximal photostriction values for different compounds. Following the work of Kundys [21], a photostrictive coefficient $\eta = d * \varepsilon/F$ is introduced to evaluate the photostrictive efficiency of different compounds at a fixed excitation photon energy, where $d$, $\varepsilon$, and $F$ are the film thickness, the absorbed laser fluence, and the measured maximum of photoinduced strain, respectively. Hence, there is no doubt that the BM-SCO film has the largest maximal strain and the highest photostrictive efficiency (not to mention that the BM-SCO data in Table I are based on the ps-resolution synchrotron work), so the acoustic phonon effect will contribute an additional 40% increase to the current value.

Generally, the underlying physics of the photostriction materials can be ascribed to the thermal elasticity, the photoinduced electrostriction, the inverse piezoelectric effect, and the deformation potential mechanism and so on [21,22]. The photostrictive effect in most ferroelectric thin films, such as $BiFeO_3$ and $PbTiO_3$, is generally attributed to the inverse piezoelectric effect modulated by the photoexcited carriers [15–17]. Recently, giant photostrictions higher than 1% were also observed in $SrRuO_3$ and $SrIrO_3$ systems via power-dependent Raman scattering and were determined to be the strong nonequilibrium electron-phonon coupling [23,24]. However, due to the complexity of the coupling between the structure and electronic states, the possible mechanisms cannot be exhausted in one single work. For example, the ultrafast photoinduced strain in the $BiFeO_3$ thin film has also

TABLE I. Comparison of photoinduced strain for different transition metal oxide films.

| Compounds | Film thickness $d$ (nm) | Laser fluence $F$ (mJ/cm$^2$) | Maximal strain $\varepsilon$(%) | Photostrictive coefficient $\eta$ | Reference |
|---|---|---|---|---|---|
| BiFeO$_3$ | 35 | 2 | 0.46 | 8 | [16] |
| PbTiO$_3$ | 20 | 1 | 0.25 | 5 | [15] |
| Sr$_2$IrO$_4$ | 20 | 3 | 0.05 | 0.3 | [14] |
| BM-SCO | 46 | 3 | 1.1 | 17 | – |

been interpreted as a characteristic of a self-trapped charge transfer exciton with a hole in the O-2$p$ orbitals and an extra electron in the Fe-3$d$ orbitals [25]. Such a self-trapped charge transfer exciton in oxides has been proposed as an inherent material property of which the hopping is facilitated by the lattice distortion, e.g., Sr$_2$IrO$_4$ thin film [14].

Regarding the giant photoinduced strain, as well as the ultrafast dynamics of coherent acoustic phonons in BM-SCO, we will discuss several potential origins in the following. Several other effects, e.g., the excitionic effect, and the polaronic effect are beyond the scope of this work but are of great interest for further investigation.

## A. Deformation potential by density functional theory calculation

The electronic distribution of the sample will be modified once the photoinduced carriers are introduced, inducing a modification of the interatomic forces. The lattice will then be deformed, emitting an acoustic phonon [22,26]. To reveal the microscopic mechanism of the giant lattice response, we simulated the photostriction effect of the photoexcited electron-hole pairs using the $\Delta$-self-consistent field (SCF) method [27]. The method fixes the occupations of certain states by taking some electrons from the valence band to the conduction band and has been applied to the studies of the photostriction effect in ferroelectric and multiferroic structures recently [28,29].

The DFT code Abinit (v8.6) [30] was employed to calculate the lattice and electronic properties. Plane waves with the energy cutoff of 30 Hartree are used as the basis set. The generalized gradient approximation–Perdew-Burke-Ernzerhof–exchange-correlation density functional [31] and projector augmented wave [32] potentials from the JTH dataset (v1.1) [33] are used. A Hubbard-U correction [34] with U(Co) = 3.5 eV [3] is applied to reproduce the $d$-$d$ and $p$-$d$ transition optical spectrum. An $8 \times 8 \times 3$ nonshifted $k$-point grid is used to integrate the Brillouin zone. The BM-SCO structure has the *Ima*2 space group and G-type antiferromagnetic order. The structures are relaxed until the residual forces are below $1 \times 10^{-6}$ Ha/Bohr ($5.14 \times 10^{-5}$ eV/A). The occupations of a pair of bands in valence and conduction bands were fixed to 1-$n_e$ and $n_e$, respectively, to mimic the electron-hole pairs with density of $n_e$. We consider the density in the dilute limit to keep the band structure almost unchanged so that it can be considered as a perturbation. All the band energy shift throughout the Brillouin zone are within 0.05 eV. The densities of CT ranging from 0 to about $2 \times 10^{20}$ cm$^{-3}$ were considered. We did not choose any specific $k$ point for the electron transfer but fixed the occupation of two bands in

the whole Brillouin zone and then relaxed the structures with the band occupations fixed.

We selected a few bands to represent the (I) O 2$p$, (II) Co 3$d$ (at the valence band maximum), (III) Co$^O$ 3$d$, and (IV) Co$^T$ 3$d$, with energies levels of about $-1.5$ eV, $-0.2$ eV, 1.0 eV, and 1.5 eV relative to the Fermi energy, respectively [Fig. 4(a)]. The II → III transfer corresponds to the $d$-$d$ transfer. Two kinds of $p$-$d$ transfer: O 2$p$ to 3$d$ in Co$^O$ (I → III) and Co$^T$ (I → IV) are considered, respectively. The results in Fig. 4(b) show that there is a distinct expansion of $c$ axis with the $p$-$d$ CT, whereas no significant change is found with the $d$-$d$ CT, which can explain the strong experimental photon energy dependence of photostriction shown in Fig. 2(d). Note that the $\Delta$-SCF method is a perturbation calculation and cannot be applicable to much higher electron density (or laser fluence), but the linear dependence of the lattice change on the concentration of excited electrons in Fig. 4(b) is consistent with the fluence-dependent results in Fig. 2(d), which attests the relevance of our numerical and experimental results. The small compression at small $d$-$d$ charge transfer in Fig. 4(b) is likely due to the limitation in the computation precision.
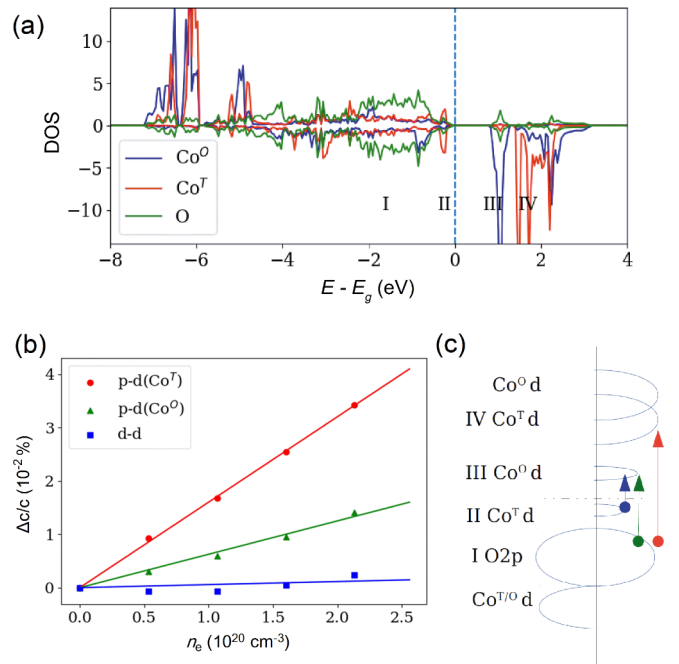


FIG. 4. (a) The density of states projected on Co 3$d$ and O 2$p$ orbitals. (b) The expansion of the $c$-axis lattice versus the density of electron-hole pairs and the schematic transfers. (c) Schematic band diagram of BM-SCO and three transitions.

TABLE II. Bond lengths and bond angles. The unit of bond lengths is Å; unit of bond angle is degree. All the bond lengths are along the $c$ direction. The results were calculated with $2.2 \times 10^{20}$ cm$^{-3}$.

| | $l$ (Co$^T$-O) | $l$ (Co$^O$-O) | $\angle$(Co$^T$ - O-Co$^O$) | $l^T$ | $l^O$ | $l^T + l^O$ |
|---|---|---|---|---|---|---|
| Pristine | 1.8210 | 2.1684 | 154.186 | 4.3417 | 3.3978 | 7.7395 |
| $p$-$d$ (Co$^O$) | 1.8207 | 2.1696 | 154.126 | 4.3436 | 3.3970 | 7.7406 |
| $p$-$d$ (Co$^T$) | 1.8237 | 2.1654 | 154.382 | 4.3413 | 3.4001 | 7.7414 |

The deformation can be seen as a response to the stress induced change of band occupation, which can be estimated by $\Delta c = -S_{33} * \Delta n_e * \frac{dE_g}{d\eta3}$, where $S_{33}$ is the elastic compliance, $\Delta n_e$ is the excited electron density, and $dE_g$ is the energy gap between the initial and final excited electron state, $\eta_3$ is the strain [26,35]. In this approximation only the band energy shift is considered whereas the change due to exchange-correlation and dipole-dipole interaction are partially neglected. The values of $\frac{dE_{g,Co-Co}}{d_{\eta3}}$, $\frac{dE_{g,\,O-CoT}}{d_{\eta3}}$, and $\frac{dE_{g,O-CoO}}{d\eta3}$ are 2.2, $-9.8$, and $-4.9$ eV, respectively. The elastic compliance $S_{33} \approx 10^{-2}$ GPa$^{-1}$ is estimated from the $C_{33} = 92 \sim 106$ GPa (experimental data) [13]. The slopes of $\Delta c / \Delta n_e$ for three CT cases estimated from the deformation potential are thus $-2.2(1.2)$, $9.8(11.1)$, and $4.9$ (4.16), with the unit of $10^{-2}$ eV/GPa. The values in the brackets are the $\Delta$−SCF results derived from Fig. 4(b). It can be seen that the estimated amplitude qualitatively agrees with the $\Delta$-SCF results in the O-Co$^T$ and O-Co$^O$ cases. It has the opposite sign in the Co-Co case, which implies that the potential deformation effect is due to other effects. In BiFeO$_3$ and PbTiO$_3$ structures, the inverse piezoelectric effect plays an important part in the photostriction [28,29]. While there is no piezoelectricity in BM-SCO, the internal electric field could have a similar effect. Electron transfer from Co$^T$ to Co$^O$ enhances the electric field shown in Fig. 1(a), which could be the reason for the lattice elongation. Also the electron-electron interaction could be strong due to the Mottness.

In the light of the DFT simulation and the estimation based on the experimental data, it is the CT of O-Co$^T$ or O-Co$^O$ via photoexcitation that plays essential parts to the photostriction. Moreover, it is more likely that the formation of the antibonding state of the O 2$p$ and Co 3$d$ (Co$^T$) via photoexcitation leads to the expansion of the Co-O bonds. The electrons occupying the antibonding state would reduce the energy gain by forming the Co-O bonds, leading to the bond expansion. Indeed, we found that with the electron transferring to the Co$^O$ (Co$^T$) state, the Co$^O$-O (Co$^T$ -O) bonds expand, as shown in Table II.

## B. Thermal contribution

Then we evaluate the contribution of thermal expansion in BM-SCO via $\varepsilon_u = \beta_{\text{eff}} * \Delta T$, where $\Delta T$ is the transient lattice temperature change and $\beta_{\text{eff}}$ refers to the effective thermal expansion coefficient of BM-SCO [36]. To experimentally determine the effective thermal expansion coefficient of the BM-SCO thin film, we first measured the Bragg peak shifts of (008) reflection at different temperatures from 25 °C to 650 °C. The measured equilibrium linear expansion coefficient is $\beta$ is $1.96 \times 10^{-5}$ K$^{-1}$ [37]. However, the

effective expansion coefficient for the UXRD experimental case is valid only if it is corrected according to the Poisson effect. In the temperature-dependent XRD measurements both the BM-SCO film and the LAO substrate were heated, but only the thin film will be heated by the laser excitation in the UXRD case. In this one-dimensional situation, the film can only expand in the out-of-plane direction because of the clamp effect induced by the substrate. The in-plane expansion of the film is prohibited and the concomitant out-of-plane contraction due to the Poisson effect vanishes, leading to an underestimated out-of-plane strain than the equilibrium case. The actual ultrafast strain should be larger by a factor of $(\frac{2c_{13}}{c_{33}}\beta_{\text{in}} + \beta_{\text{out}})$ [36], where $c_{13}$ and $c_{33}$ are components of the elastic strain tensors, $\beta_{\text{in}}$ and $\beta_{\text{out}}$ are the linear expansion coefficients along the in- and out-of-plane directions. Hence, a more realistic expansion coefficient is obtained to be $5.79 \times 10^{-5}$ K$^{-1}$, almost 3 (2.95) times larger than the equilibrium case. Here we assume $\beta_{in} \approx \beta_{\text{out}} = 1.96 \times 10^{-5}$ K$^{-1}$.

The lattice temperature changes $\Delta T$ could be obtained via $\Delta T = \Delta Q / C_p \rho D$, where $\Delta Q$, $C_p$, $\rho$, and $D$ refer to the deposited energy, specific heat, density, and film thickness, respectively. From the microscopic point of view, only the excessive energy of the excitation photons ($E_a$-$E_g$) will be transferred to the lattice through electron-phonon interaction and increase the thermal phonons population, thus to induce a temperature increase $\Delta T$. The calculation does not account for the interband relaxation process, since the nonradiative recombination is not the dominated process [17,22,26], as indicated by the linear dependence of the strain on the fluence [Fig. 2(d)]. Therefore, only part of the absorbed energy, $(E_a - E_g)/E_a$, will be converted into heat and the transient temperature increase is calculated by use of $\Delta T = F_{\text{abs}}(E_a - E_g)/C_p \rho D E_g$, where $F_{\text{abs}}$ is the absorbed laser fluence and could be obtained from the incident fluence $F_p$ by $F_{\text{abs}} = F_p(1 - R)[1 - \exp(-\alpha D/\cos\theta]$ [17]. With the parameters given in Appendix A, the temperature jump is calculated to be 26.7 K for the 1.55 mJ/cm$^2$, 3.1 eV pump pulses. The corresponding thermal expansion is estimated to be 0.154%, which stands for 38% of the total photoinduced strain of 0.404% at 150 ps time delay. Overall, the thermal expansion introduced by the photoexcitation does play an important part in the photostriction effect, but is still insufficient to account for the actual magnitude of the observed strain, especially at sub-100 ps time scales.

## C. Screening of internal electric field

Another possibility is the modification of the internal electric field via the optical generation of CT in BM-SCO. Though BM-SCO is nonferroelectric, there exists an electric field pointing from (Co$^T$O)$^+$ layers to (Co$^O$O$_2$)$^-$ layers, due to

the layered $(Co^T O)^+ - (SrO) - (Co^O O_2)^- - (SrO)$ structure, as shown in Fig. 1(a). The $Sr^{2+}$ ions are attracted by the $(Co^O O_2)^-$ layer, reducing the distance of Sr-Sr with $Co^O$ (denoted as $l^O$) and increasing the Sr-Sr distance with $Co^T$ (denoted as $l^T$), resulting in an extremely large $c/a$ in the pristine BM-SCO film. The Sr-Sr distances along the $c$ axis are ideal to detect the change of the field. However, under this scheme, the $p$-$d$ ($Co^T$) CT will shrink the lattice along the $c$ direction, while $p$-$d$ ($Co^O$) CT will expand the lattice, inconsistent with our calculation where the $p$-$d$ ($Co^T$) CT indicates a much larger expansion than $p$-$d$ ($Co^O$) CT [Fig. 4(b) and Table I]. Thus the photostriction in BM-SCO is not attributed to the inverse piezoelectric effect.

### D. High spin to intermediate spin crossover

We also calculated the structure of BM-SCO with high, low, and intermediate spin state to see whether the spin crossover effect can lead to a $c$-axis expansion. In the ground state of the high spin state, the electronic configurations of both the $Co^O$ and $Co^T$ ions are $d^5 \uparrow d^1 \downarrow$; in the low spin state, they become $d^3 \uparrow d^3 \downarrow$. We found that the $Co^O$ ion has an energy local minimum with $d^4 \uparrow d^2 \downarrow$, whereas $Co^T$ will stay high spin. The $d$-$d$ charge transfer is from the occupied minor spin channel to the unoccupied orbital in the same spin channel. Since the major spin channel is fully occupied, the spin crossover is not possible. Whereas the $p$-$d$ transfer would allow the spin crossover since the major spin channel is hybridized with O $2p$. A large $c$-axis elongation can be found in the intermediate spin state due to the strong Jahn-Teller effect of the state $d^4 \uparrow d^2 \downarrow Co^O$ (Appendix B).

However, we note that the characteristic oscillation frequency of an ultrafast spin crossover system is generally on the order of THz [24,37], inconsistent with our optical pump-probe spectroscopy (which is only about 30 GHz). As a result, the photoexcited spin crossover effect could be precluded for the origin of giant photostriction.

## IV. CONCLUSION

In summary, we combine the multitimescale UXRD experiments and DFT computation to investigate the photoinduced strain in an oxygen-ordered SCO film. The giant lattice distortion with a strong photon energy dependence has been observed. This phenomenon is likely attributed to the photoexcitation of bonding to antibonding state via CT, which

results in the bond expansion in the SCO unit cells. The photoinduced thermal phonons can also contribute to the large expansion. The integration of ps- and fs- UXRD measurements, complemented by the recent application of $\Delta$-SCF calculations on simulating the photostriction effect, helps to rejuvenate the photophysics research in functional materials. The giant lattice distortion might be inherent for other oxides with oxygen vacancies to induce large tetragonality. The manipulation of the supertetragonality via photoexcited carriers may offer a promising route to tailoring the material properties and functionalities such as piezoelectricity or electrostriction.

## APPENDIX A

The Appendix A summarizes the parameters of the BM-SCO for the estimation of thermal contribution.

| | | |
|---|---|---|
| Incident laser fluence $F_p$ | 1.55 | mJ/cm$^2$ |
| Reflectivity $R$ (400 nm) | 0.22 | N.A. |
| Reflectivity $R$ (800 nm) | 0.1 | N.A. |
| Film thickness $D$ | 46 | Nm |
| Absorption coefficient $\alpha$ (400 nm) | 0.034 | nm$^{-1}$ |
| Absorption coefficient $\alpha$ (800 nm) | 0.01 | nm$^{-1}$ |
| Mott band gap $E_{g1}$ | 0.45 | eV |
| Direct band gap $E_{g2}$ | 2.18 | eV |
| Laser incident angle $\theta$ | 45 | degree |
| Density $\rho$ | 5.2 | g/cm$^3$ |
| Thermal expansion coefficient $\beta$ | $5.79 \times 10^{-5}$ | K$^{-1}$ |
| Specific heat per unit mass $c$ | 0.5 | J/(g $\ast$ K) |

## APPENDIX B

Lattice parameters of BM-SCO with various spin configurations.

| Spin state | $a$(Å) | $b$(Å) | $c$(Å) | Volume (Å$^3$) | mCo$^T$($\mu$B) | mCo$^O$($\mu$B) |
|---|---|---|---|---|---|---|
| High | 5.3599 | 5.3599 | 15.9037 | 456.8856 | 2.86 | 2.91 |
| Intermediate | 5.3599 | 5.3599 | 15.9719 | 458.8451 | 2.87 | 2.24 |
| Low | 5.3599 | 5.3599 | 15.1620 | 435.5760 | 0.00 | 0.00 |

[1] J. B. Goodenough, Rep. Prog. Phys. **67**, 1915 (2004).

[2] J. Suntivich, H. A. Gasteiger, N. Yabuuchi, H. Nakanishi, J. B. Goodenough, and Y. Shao-Horn, Nat. Chem. **3**, 546 (2011).

[3] W. S. Choi, H. Jeen, J. H. Lee, S. S. Ambrose Seo, V. R. Cooper, K. M. Rabe, and H. N. Lee, Phys. Rev. Lett. **111**, 097401 (2013).

[4] H. Jeen, W. S. Choi, M. D. Biegalski, C. M. Folkman, I. C. Tung, D. Fong, J. W. Freeland, D. Shin, H. Ohta, M. F. Chisholm, and H. N. Lee, Nat. Mater. **12**, 1057 (2013).

[5] Q. Y. Lu, Y. Chen, H. Bluhm, and B. Yildiz, J. Phys. Chem. C **120**, 24148 (2016).

[6] H. Jeen, W. S. Choi, J. W. Freeland, H. Ohta, C. U. Jung, and H. N. Lee, Adv. Mater. **25**, 3651 (2013).

[7] R. Le Toquin, W. Paulus, A. Cousson, C. Prestipino, and C. Lamberti, J. Am. Chem. Soc. **128**, 13161 (2006).

[8] E. Bousquet, M. Dawber, N. Stucki, C. Lichtensteiger, P. Hermet, S. Gariglio, J.-M. Triscone, and P. Ghosez, Nature (London) **452**, 732 (2008).

[9] S. J. Callori, S. Hu, J. Bertinshaw, Z. J. Yue, S. Danilkin, X. L. Wang, V. Nagarajan, F. Klose, J. Seidel, and C. Ulrich, Phys. Rev. B **91**, 140405(R) (2015).

[10] J. Zhao, H. Guo, X. He, X. Li, K. Jin, C. Ge, M. He, Y. Long, J. Wang, H. Qian, C. Wang, H. Lu, G. Yang, and K. Ibrahim, ACS Appl. Mater. Interface. **10**, 10211 (2018).

[11] F. Hong, B. B. Yue, Z. X. Liu, B. Chen, and H. K. Mao, Phys. Rev. B **95**, 024115 (2017).

[12] Q. Y. Lu and B. Yildiz, Nano Lett. **16**, 1186 (2016).

[13] N. P. Lu, P. F. Zhang, Q. H. Zhang, R. M. Qiao, Q. He, Hao-Bo Li, Y. J. Wang, J. W. Guo, D. Zhang, Z. Duan, Z. L. Li, M. Wang, S. Z. Yang, M. Z. Yan, E. Arenholz, S. Y. Zhou, W. L. Yang, L. Gu, Ce-Wen Nan, J. Wu, Y. Tokura, and P. Yu, Nature (London) **546**, 124 (2017).

[14] Y. L. Li, R. D. Schaller, M. Z. Zhu, D. A. Walko, J. Kim, X. L. Ke, L. D. Miao, and Z. Q. Mao, Sci. Rep. **6**, 19302 (2016).

[15] D. Daranciang, M. J. Highland, H. D. Wen, S. M. Young, N. C. Brandt, H. Y. Hwang, M. Vattilana, M. Nicoul, F. Quirin, J. Goodfellow, T. Qi, I. Grinberg, D. M. Fritz, M. Cammarata, D. Zhu, H. T. Lemke, D. A. Walko, E. M. Dufresne, Y. Li, J. Larsson, D. A. Reis, K. Sokolowski-Tinten, K. A. Nelson, A. M. Rappe, P. H. Fuoss, G. B. Stephenson, and A. M. Lindenberg, Phys. Rev. Lett. **108**, 087601 (2012).

[16] D. Schick, M. Herzog, H. Wen, P. Chen, C. Adamo, P. Gaal, .D. G. Schlom, P. G. Evans, Y. Li, and M. Bargheer, Phys. Rev. Lett. **112**, 097602 (2014).

[17] H. Wen, P. Chen, M. P. Cosgriff, D. A. Walko, J. H. Lee, C. Adamo, R. D. Schaller, J. F. Ihlefeld, E. M. Dufresne, D. G. Schlom, P. G. Evans, J. W. Freeland, and Y. Li, Phys. Rev. Lett. **110**, 037601 (2013).

[18] B. Zhang, S. Sun, D. Sun, and Y. Tao, Rev. Sci. Instrum. **85**, 096110 (2014).

[19] D. Schick, R. Shayduk, A. Bojahr, M. Herzog, C. K. Schmising, P. Gaal, and M. Bargheer, J. Appl. Cryst. **46**, 1372 (2013).

[20] D. Schick, M. Herzog, A. Bojahr, W. Leitenberger, A. Hertwig, R. Shayduk, and M. Bargheer, Struct. Dynam. **1**, 064501 (2014).

[21] B. Kundys, Appl. Phys. Rev. **2**, 011301 (2015).

[22] P. Ruello and V. E. Gusev, Ultrasonics **56**, 21 (2015).

[23] T. Wei, H. Wang, H. Liu, D. Tsai, J. Ke, C. Wu, Y. Yin, Q. Zhan, G. Lin, Y. Chu, and J. He, Nat. Commun. **8**, 15108 (2018).

[24] J. Yang, Y. Liou, W. Tzeng, H. Liu, Y. Chang, P. Xiang, Z. Zhang, C. Duan, C. Luo, Y. Chen, and Y. Chu, Nano Lett. **18**, 7742 (2018).

[25] Y. Li, C. Adamo, C. E. Rowland, R. D. Schaller, D. G. Schlom, and D. A. Walko, APL Mater. **6**, 084905 (2018).

[26] C. Thomsen, H. T. Grahn, H. J. Maris, and J. Tauc, Phys. Rev. B **34**, 4129 (1986).

[27] R. M. Martin, *Electronic Structure: Basic Theory and Practical Methods* (Cambridge University Press, Cambridge, UK, 2004).

[28] Y. R. Yang, C. Paillard, B. Xu, and L. Bellaiche, J. Phys.: Condens. Matter **30**, 073001 (2018).

[29] C. Paillard, B. Xu, B. Dkhil, G. Geneste, and L. Bellaiche, Phys. Rev. Lett. **116**, 247401 (2016).

[30] X. Gonze, B. Amadon, P. M. Anglade, J. M. Beuken, F. Bottin, P. Boulanger, F. Bruneval, D. Caliste, R. Caracas, M. Côté, T. Deutsch, L. Genovese, Ph. Ghosez, M. Giantomassi, S. Goedecker, D. R. Hamann, P. Hermet, F. Jollet, G. Jomard, S. Leroux, M. Mancini, S. Mazevet, M. J. T. Oliveira, G. Onida, Y. Pouillon, T. T. Rangel, G.-M. Rignanese, D. Sangalli, R. Shaltaf, M. Torrent, M. J. Verstraete, G. Zerah, and J. W. Zwanziger, Comput. Phys. Commun. **180**, 2582 (2009).

[31] J. P. Perdew, A. Ruzsinszky, G. I. Csonka, O. A. Vydrov, G. E. Scuseria, L. A. Constantin, X. L. Zhou, and K. Burke, Phys. Rev. Lett. **100**, 136406 (2008).

[32] M. Torrent, F. Jollet, F. Bottin, G. Zerah, and X. Gonze, Comp. Mater. Sci. **42**, 337 (2008).

[33] F. Jollet, M. Torrent, and N. Holzwarth, Comput. Phys. Commun. **185**, 1246 (2014).

[34] A. I. Liechtenstein, V. I. Anisimov, and J. Zaanen, Phys. Rev. B **52**, R5467 (1995).

[35] C. Paillard, S. Prosandeev, and L. Bellaiche, Phys. Rev. B **96**, 045205 (2017).

[36] J. Pudell, A. A. Maznev, M. Herzog, M. Kronseder, C. H. Back, G. Malinowski, A. von Reppert, and M. Bargheer, Nat. Commun. **9**, 3335 (2018).

[37] H. Chu, L. Zhao, A. de la Torre, T. Hogan, S. D. Wilson, and D. Hsieh, Nat. Mater. **16**, 200 (2017).